catalysts

MDPI

Article

Au Supported on Bovine-Bone-Derived Hydroxyapatite Catalyzes CO_2 Photochemical Reduction toward Methanol

Sergio Arturo Gama-Lara [1], Alfredo Rafael Vilchis-Néstor [2], Deysi Amado-Piña [2] and Reyna Natividad [2,*]

[1] Engineering Department, CIIDETEC-Toluca, Universidad del Valle de México, Toluca 52164, Mexico; gamaliel350@gmail.com
[2] Centro Conjunto de Investigación en Química Sustentable UAEM-UNAM, Carretera Toluca-Atlacomulco Km. 14.5, San Cayetano, Toluca 50200, Mexico; arvilchisn@uaemex.mx (A.R.V.-N.); damadop_ext@uaemex.mx (D.A.-P.)
* Correspondence: rnatividadr@uaemex.mx

Abstract: In this work, gold-photo-catalyzed CO_2 transformation was conducted and the effect of three variables with two levels was investigated: support (TiO_2 and hydroxyapatite from bovine bone (BB)), Au content (5 and 10%) and activation wavelength (254 and 380–700 nm). Reactions were conducted in a stirred tank reactor by bubbling CO_2 (9×10^{-3} dm^3/min) in 0.1 dm^3 of 0.5 M NaOH solution. The catalysts were synthesized using $AuCl_3$, TiO_2 and BB. Au nanoparticles were obtained by reduction with *Hetheroteca inuloides*, thus eliminating calcination and hydrogenation to reduce the gold species. By TEM, the particle size distribution was determined, and the synthesized nanoparticle sizes varied in the range of 9 to 19 nm, depending on the support and Au content. By UV–Vis spectroscopy, the energy band gaps of the prepared materials were 2.18 eV (10% Au/BB), 2.38 eV (5% Au/BB), 2.42 eV (BB), 3.39 eV (5% Au/TiO_2), 3.41 eV (10% Au/TiO_2) and 3.43 eV for pure TiO_2. Methanol and formic and acetic acids were identified during the process. Selectivity toward methanol was found to be improved with the 10% Au/BB catalytic system.

Keywords: carbon dioxide; CO_2 photoreduction; hydroxyapatite; gold photocatalysis; Au/TiO_2; methanol production; formic acid; acetic acid; plasmon-driven photocatalysis

Citation: Gama-Lara, S.A.; Vilchis-Néstor, A.R.; Amado-Piña, D.; Natividad, R. Au Supported on Bovine-Bone-Derived Hydroxyapatite Catalyzes CO_2 Photochemical Reduction toward Methanol. *Catalysts* **2024**, *14*, 417. https://doi.org/10.3390/catal14070417

Academic Editors: Bo Weng and Akira Nishimura

Received: 19 April 2024
Revised: 19 June 2024
Accepted: 24 June 2024
Published: 29 June 2024

1. Introduction

In the last decade, Carbon dioxide (CO_2) chemical reduction has been increasingly studied as a response to mitigate CO_2 emissions, and thus, their inherent anthropogenic effect. This can be conducted by different means, i.e., thermochemical, electrochemical, photochemical or by their combination. By any of these, the outcome is molecules that serve either as fuels (methanol, ethanol, formic acid) or as feed stock molecules, i.e., acetic acid. A common challenge is the selectivity and yield of any of these. This challenge, in the context of the photochemical transformation of CO_2, has been extensively addressed, mainly by modifying the photocatalyst surface with transition metals. The preferred photocatalyst, as in many other applications, is TiO_2. Nevertheless, the scientific community has dedicated special effort to finding alternative catalytic systems to improve the yield and selectivity toward added-value chemicals. In this sense, hydroxyapatite (HAP) has been recently reported [1–3] to be an interesting support and catalyst to aid the CO_2 conversion driven by light.

HAP, $Ca_5(PO_4)_3(OH)$, is a material that can be either synthesized in the laboratory or can be found as a main component of biomaterials, such as bovine bones. An important characteristic of this material for its use as a catalytic support is that the functional groups attract and anchor the metallic ions to the surface. This characteristic has been used in photocatalysis to make HAP active in the visible spectrum with the addition of metals like Fe, Cu and Co [4–7]. In the area of photocatalysis, HAP has been mainly used for organics oxidation.

In the conversion of CO_2, the catalytic activity of HAP-based catalysts has been demonstrated in hydrogenation reactions [8] and the photocatalytic activity of HAP and polarized HAP has been recently demonstrated alone and by supporting TiO_2 nanoparticles [9] and metallic particles [10]. So far, the aspects that have been found relevant for the use of HAP in the conversion of CO_2 are its selectivity, its high degree of -OH functionalization and that it is a naturally occurring mineral [1,2]. These works, which are very recent, however, were performed in the gas phase, with UV light, using a moderate temperature (95 °C) and some with polarized synthetic (not natural) HAP. The procedure to polarize HAP implies the use of electrical discharges and high temperatures (1000 °C) [2], which might compromise the sustainability of the process. Based on the existing related literature, Scheme 1 summarizes the different organic compounds obtained by performing the conversion of CO_2 with p-HAP.

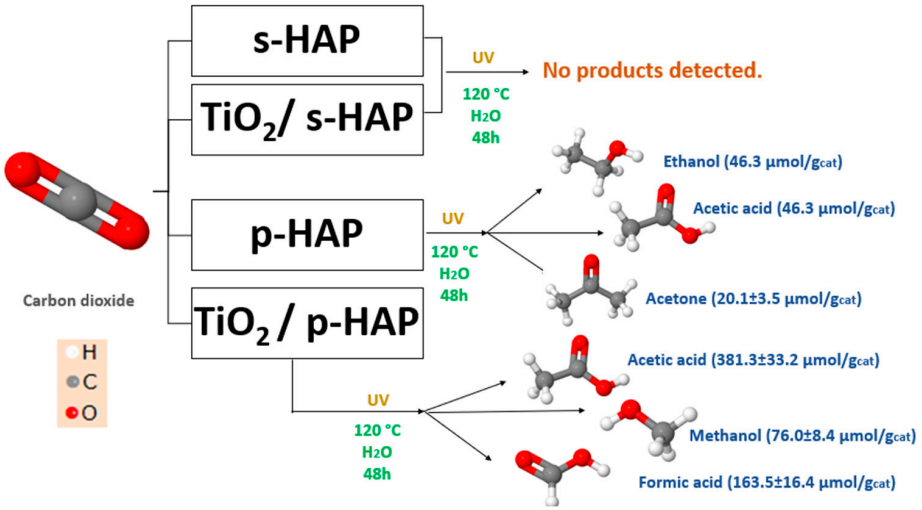

Scheme 1. Reported [1] added-value chemical compounds in the transformation of CO_2 aided by hydroxyapatite. HAP: hydroxyapatite, s-HAP: sintered HAP, p-HAP: polarized HAP.

It is worth noticing that the addition of TiO_2 nanoparticles to HAP shifted the selectivity from ethanol to acetic acid [1]. The effect of adding other nanoparticles to HAP in the conversion of CO_2 driven by light has not been unveiled. Moreover, the addition of metallic nanoparticles to HAP, albeit for other applications, was conducted via typical methods like impregnation [11,12]. The applications of HAP with nanoparticles include syngas production from dry reforming methane [12,13], selective production of alcohols from ethanol [14], lignin valorization [15] and environmental decontamination [4,5,16–21].

It was the objective of this manuscript to present the results obtained from performing the CO_2 conversion in aqueous solution, driven by light and catalytic systems constituted by gold supported on TiO_2 and HAP derived from BB, with the purpose of the comparison and elucidation of the effect of the support on the concentration and selectivity toward methanol, formic acid and acetic acid. It is important to note that bovine bone (BB) was used as the source of HAP.

To obtain nanometric systems, several methodologies have been used, such as the sol–gel method, co-precipitation, chemical methods, the Stöber method, the acid oxidative process, the thermal decomposition method and spray pyrolysis [22–25]. In recent years, special attention has been given to green synthesis methods because they are environmentally friendly, as they do not generate toxic by-products, and have certain components that improve specific properties in nanocomposites; these green methods can include bioreductors, such as fungi, plants and microorganisms [26–28]. Thus, in this work, gold nanoparticles in both systems were obtained via the chemical reduction of the gold precursor with *Hetheroteca inuloides*, thus eliminating the calcination and hydrogenation stages typically associated with the production of metallic nanoparticles. Besides the effect of the support, the effect of the light wavelength and the gold content are also presented.

Some works have been reported where bovine bone powder, mainly constituted by hydroxyapatite, was used as a support for metallic nanoparticles due to the high electronic attraction produced by its functional groups (OH^- and PO_4^{-3}) [29]; for example, silver was synthesized and its bactericidal properties were evaluated [30], and platinum was synthesized and its catalytic properties were evaluated [31].

Regarding metals and in the context of CO_2 photocatalyzed chemical reduction, the most assessed have been copper and gold [32]. What makes gold a very interesting material in photocatalysis is its surface plasmon resonance, which allows for the production of hot carriers. Such carriers can be electrons that can directly intervene in the chemical reduction of CO_2, for instance, in [33]. Plasmon hot electrons can present energies above the Fermi level of the metal [34] and this makes relevant the use of Au, as well as other plasmonic materials, like silver and copper. The use of the referred carriers to drive chemical reactions falls into a relatively new field known as plasmonic photocatalysis [33].

2. Results and Discussion

2.1. Catalysts Characterization

2.1.1. Crystallographic Structure

Figure 1 compares the patterns of BB (green), 5% Au/BB (black) and 10% Au/BB (red). In the case of bovine bone, the pattern showed signals at 2θ values of 22.88°, 25.89°, 29.17°, 32°, 33.19°, 40.14°, 46.99° and 49.66° that could be correlated with the following planes of hexagonal hydroxyapatite: (111), (002), (210), (211), (300), (130), (222) and (213), respectively (ICDD card: 00-086-0740). Likewise, the Au-NPs showed signals at 2θ value of 38.41°, 44.47°, 64.71° and 77.79° that could be correlated with the following planes of FCC Au: (111), (200), (202) and (311), respectively (ICDD card: 00-004-0783). The reflections associated with FCC Au in the BB sample were absent. However, for the 10% Au/BB sample, the reflections reached their maximum intensity, indicating a higher gold content in the sample.

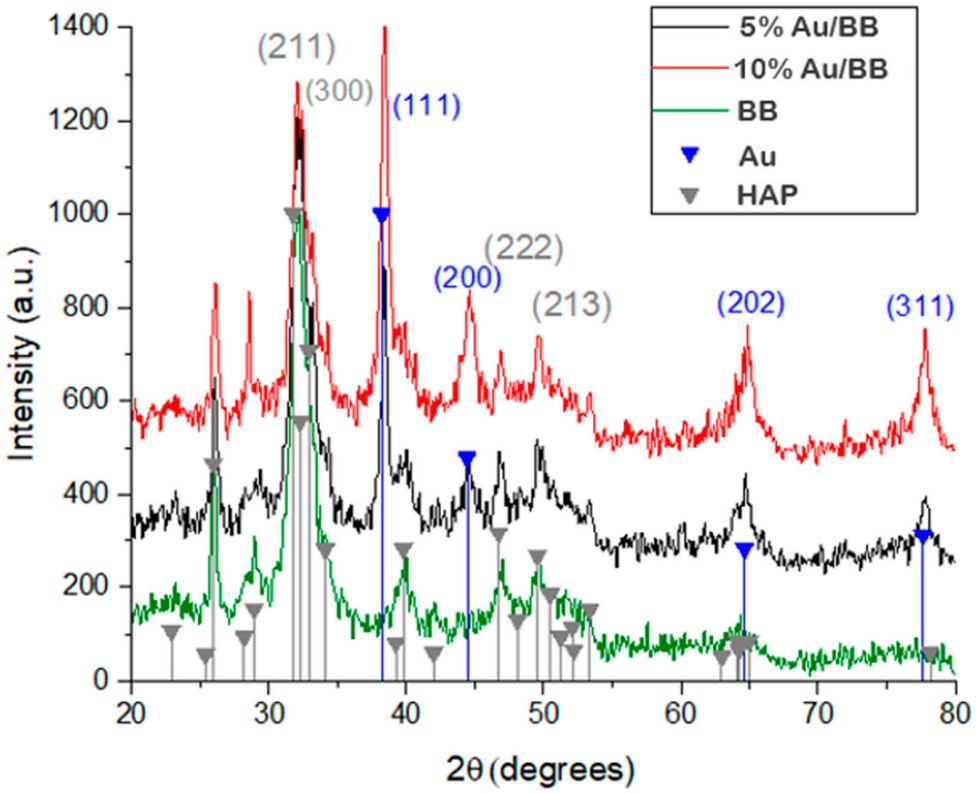

Figure 1. XRD patterns of pure BB (green), 5% Au-NPs supported on BB (black) and 10% Au-NPs supported on BB (red).

Figure 2 depicts the patterns of 5% Au/TiO_2 (blue) and 10% Au/TiO_2 (red). In the case of the support (TiO_2), the pattern showed signals at 2θ values of 25.33°, 37.82°, 48.09°, 53.93°, 55.12°, 46.99°, 68.82° and 75.12° that could be correlated with the following planes of tetragonal TiO_2 (anatase): (101), (004), (200), (105), (211), (116) and (215), respectively (ICDD card: 00-084-1286). Likewise, the Au-NPs showed signals at 2θ value of 38.41°, 44.47°, 64.71° and 77.79° that could be correlated with the following planes of FCC Au: (111), (200), (202) and (311), respectively (ICDD card: 00-004-0783). Signals of FCC Au could be observed in the 5% Au/BB sample and showed the highest peak for 10% Au/BB, showing a higher amount of gold in the sample.

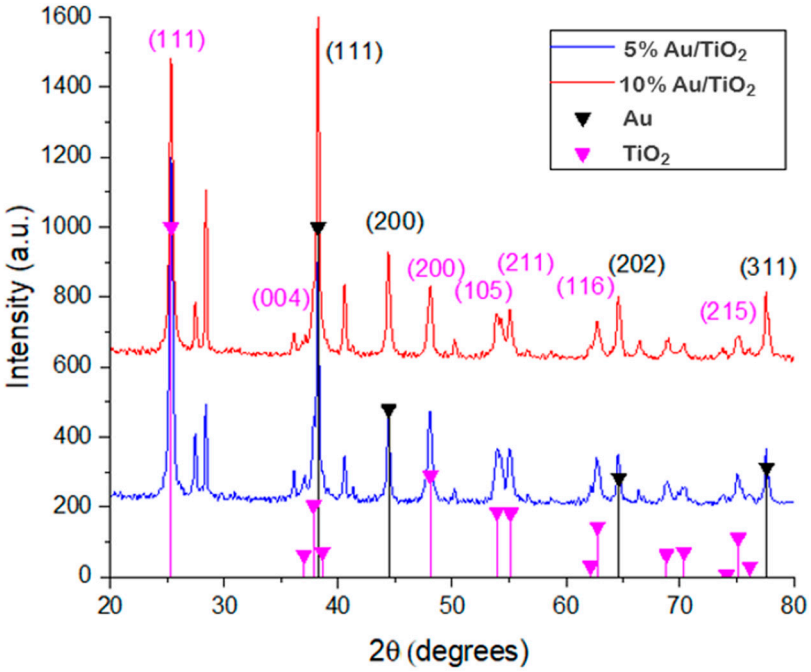

Figure 2. XRD patterns of 5% Au/TiO_2 (blue) and 10% Au/TiO_2 (red).

2.1.2. Optical Characteristics

UV–Vis spectroscopy was used to characterize the optical response of the prepared composites. Figure S1a (Supplementary Materials) shows the absorption band of 5% Au/BB (blue) being higher than the pure BB (violet) band, and the 10% Au/BB absorption band was even higher. This difference could be attributed to the presence of gold nanoparticles on the sample and their strong surface plasmon absorption. Furthermore, to determine the band gap of prepared materials, a Tauc model was used (Figure S1b,c in Supplementary Material). The 5% Au/BB band gap value was 2.38 eV (522 nm), the 10% Au/BB had 2.18 eV (570 nm) and the pure BB had 2.42 eV (513 nm); this difference meant that less energy was required to pass an electron from the valance band to the conduction band in the Au-NPs nanocomposite. It is worth noticing that these values were lower than those reported for synthetic HAP doped with Zn and Cu, for instance. In such a case, the reported value was not that different (3.3 eV) from P25 [35]. The values obtained in this work, however, are of similar magnitude to those reported for HAP doped with iron [10]. Figure S2a (Supplementary Materials) shows that the absorption band of 5% Au/TiO_2 (blue) was higher than the pure TiO_2 (violet) band and the 10% Au/TiO_2 absorption band. In a similar way than with BB, this difference could be attributed to the presence of gold nanoparticles on the sample and their surface plasmon resonance (SPR). Furthermore, to determine the band gap of the Au-NPs, the Tauc model was used (Figure S2b,c in Supplementary Material). The 5% Au/TiO_2 band gap value was 3.39 eV (366 nm), the 10% Au/TiO_2 had 3.43 eV (362 nm) and the pure TiO_2 had 3.41 eV (364 nm). It has been reported that a decrease in the band gap leads to an improvement in its photocatalytic activity [36,37].

2.1.3. Electronic Transmission Microscopy (TEM)

Figure 3 shows the chemical mapping for Au in the different systems: (a) 5% Au/BB, (b) 10% Au/BB, (c) 5% Au/TiO_2 and (d) 10% Au/TiO_2. The complete chemical mappings (not included here) show the composition of the systems. The BB support was basically composed of hydroxyapatite ($Ca_5(PO_4)_3(OH)_2$) (calcium, phosphorus, oxygen and carbon) and TiO_2 was composed of titanium and oxygen. The chemical mapping in Figure 3 shows the dispersion of gold on the support, with significant differences between supports; while the system that used bovine bone powder as a support showed a homogeneous distribution over the support, in the case of TiO_2, the presence of gold was concentrated in certain areas.

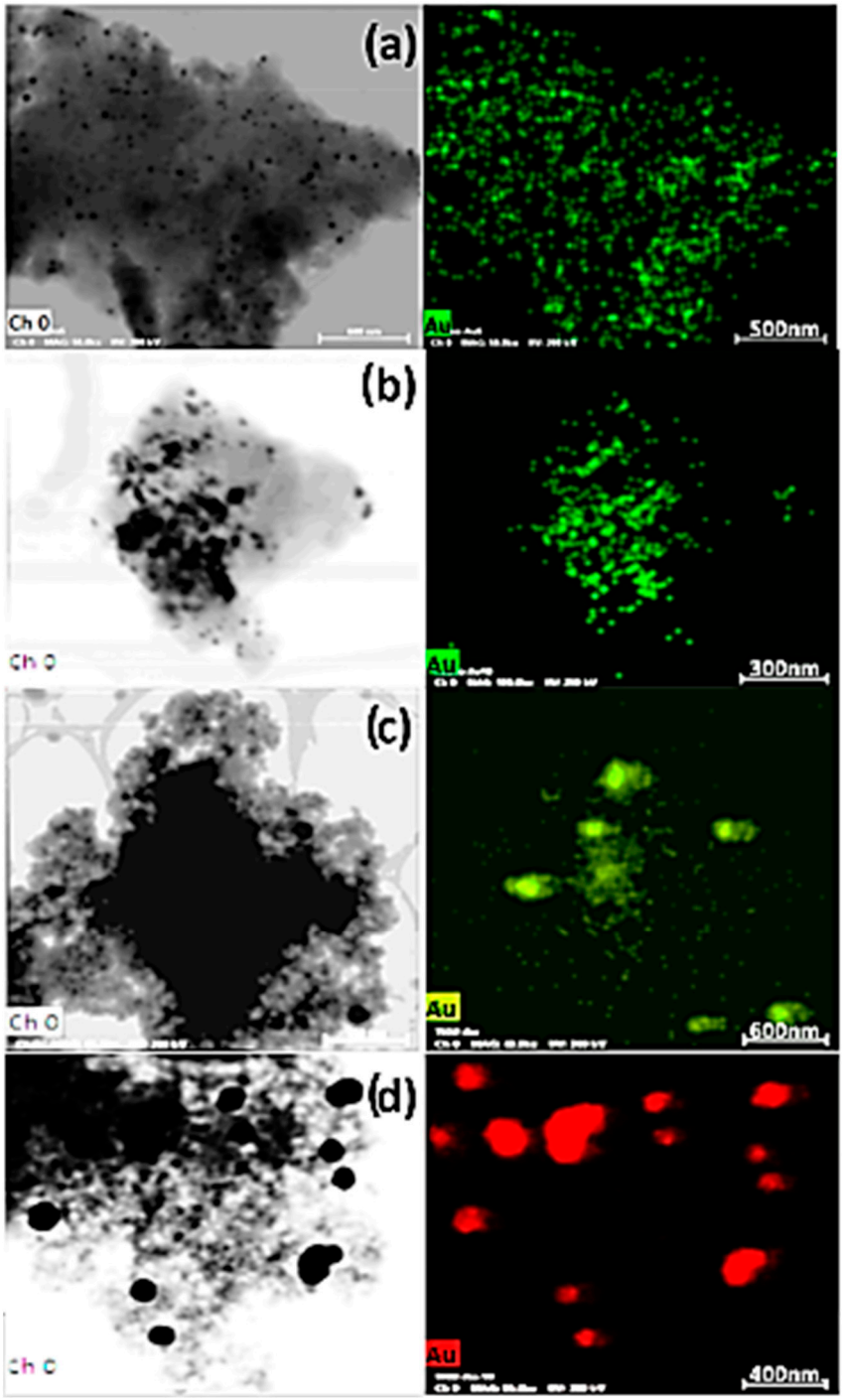

Figure 3. EDS elemental mapping of TEM of (**a**) 5% Au/BB, (**b**) 10% Au/BB, (**c**) 5% Au/TiO_2 and (**d**) 10% Au/TiO_2.

Transmission electron microscopy images (Figure 4a,b) correspond to 5% Au/BB. The support can be observed (lighter area) and over it the gold NPs (darker area), the gold particles show a good polydispersity with a size range between 4–53 nm and quasi-spherical shape. An histogram at the end of this section shows an average size of Au-NPs of 9.77 nm by the measurement of approximately 750 particles. Selected area electron diffraction (SAED) of 5% Au/BB (Figure 4d) was analyzed by measuring the interplanar distance between the atoms, the patterns corresponded to (111), (200) and (202) FCC Au lattice planes (ICDD pattern: 00-004-0784) and (002), (211) and (222) for hexagonal structure of hydroxyapatite (ICDD pattern: 00-086-0740).

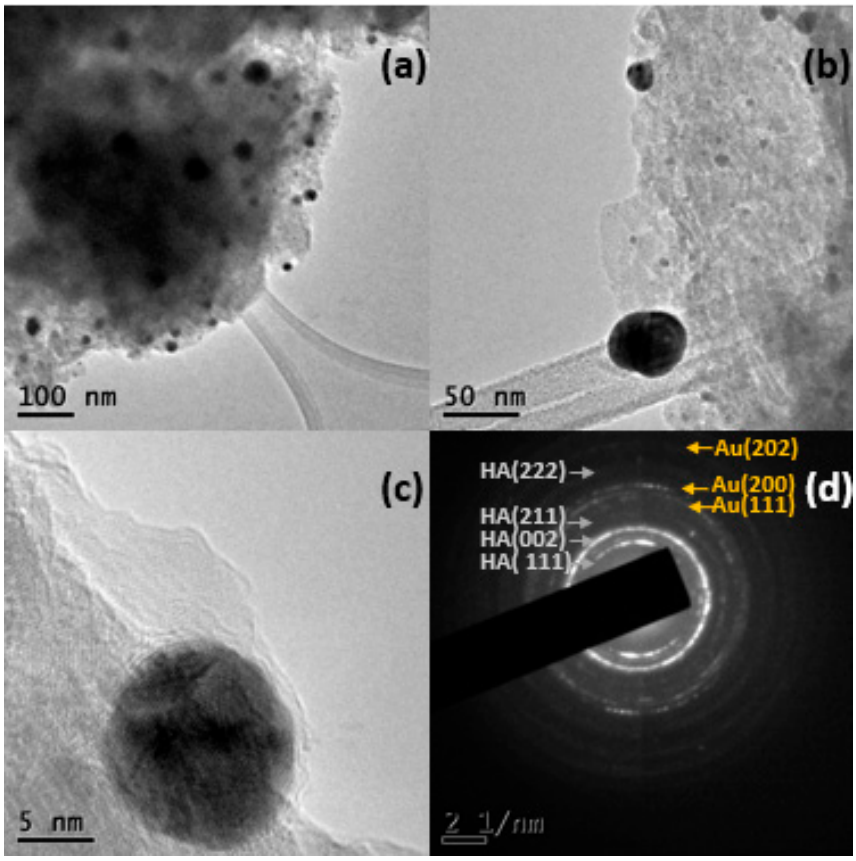

Figure 4. (**a**,**b**) TEM micrographs of 5% Au-NPs supported on BB, (**c**) Au nanoparticle on BB and (**d**) SAED pattern.

With respect to the 10% Au/BB powder system, Figure 5a,b show TEM micrographs, where the bovine bone powder (lighter area) and over it the gold NPs (darker area) are observed. The gold particles showed a good polydispersity with a size ranging between 3 and 51 nm and a quasi-spherical shape with an average size of Au-NPs of 17.96 nm. Selected area electron diffraction (SAED) of 10% Au/BB (Figure 5d) shows patterns corresponding to (111), (200) and (202) FCC Au lattice planes (ICDD pattern: 00-004-0784) and (111), (002) and (213) for the hexagonal structure of hydroxyapatite (ICDD pattern: 00-086-0740).

Regarding the system of 5% Au/TiO_2, TEM micrographs (Figure 6a,b) showed the support TiO_2 (lighter), and over it, the gold NPs (darker). The micrographs showed that approximately 5% of the particles were larger than 60 nm, up to 238 nm in size; the remaining particles showed a quasi-spherical shape with an average of 13.65 nm, where 722 particles were measured. The selected area electron diffraction (SAED) of the 5% Au/TiO_2 (Figure 6d) showed patterns correspondence to (111), (200) and (202) FCC Au lattice planes (ICDD pattern: 00-004-0784) and (111), (004), (105) and (204) anatase TiO_2 lattice planes according to a tetragonal structure (ICDD pattern: 00-084-1286).

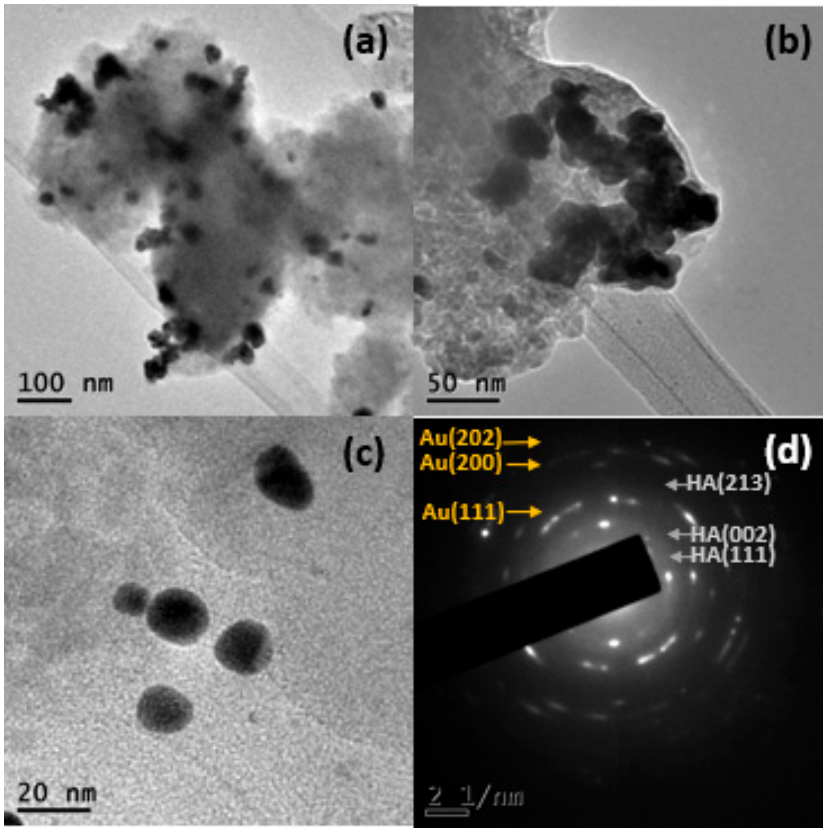

Figure 5. (**a**,**b**) TEM micrographs of 10% Au/BB, (**c**) Au nanoparticle on BB and (**d**) SAED pattern.

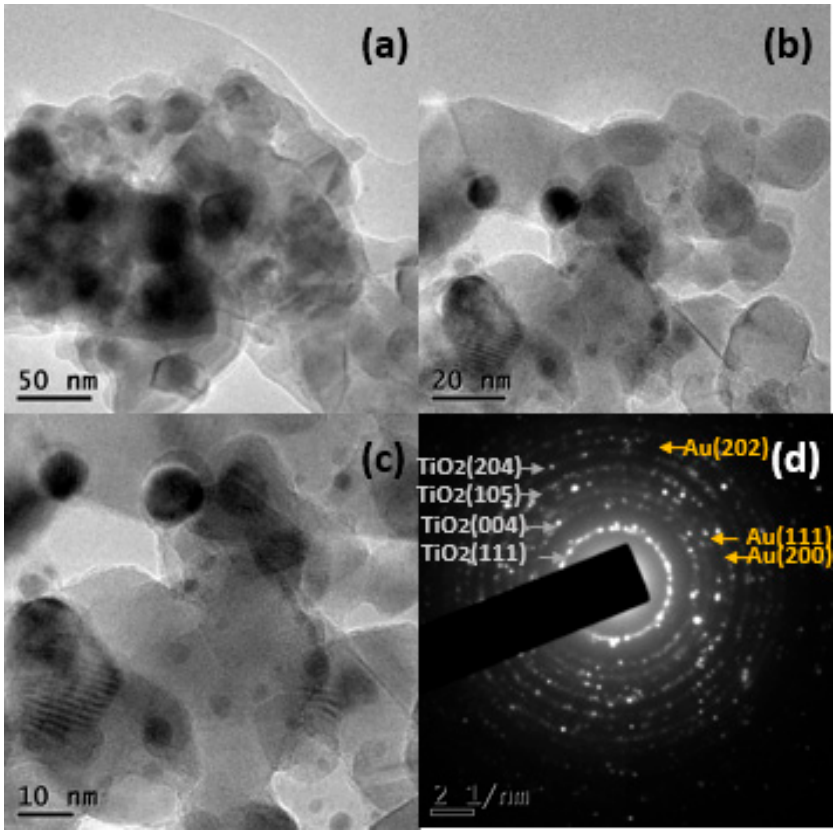

Figure 6. (**a**–**c**) TEM micrographs of 5% Au/TiO_2 and (**d**) SAED pattern.

Figure 7a,b show the TEM micrographs of 10% Au/TiO_2, with the support TiO_2 (brighter), and over it, the gold NPs (darker); the micrographs show that approximately 14% of the particles were larger than 60 nm, up to 302 nm in size, and the remaining particles showed a quasi-spherical shape with an average of 13.49 nm (Figure 8d), where 544 particles were measured. The selected area electron diffraction (SAED) of 10% Au/TiO_2 (Figure 7d) showed patterns corresponding to (111), (200) and (202) FCC Au lattice planes (ICDD pattern: 00-004-0784) and (111), (200), (105) and (204) anatase TiO_2 lattice planes according to a tetragonal structure (ICDD pattern: 00-084-1286).

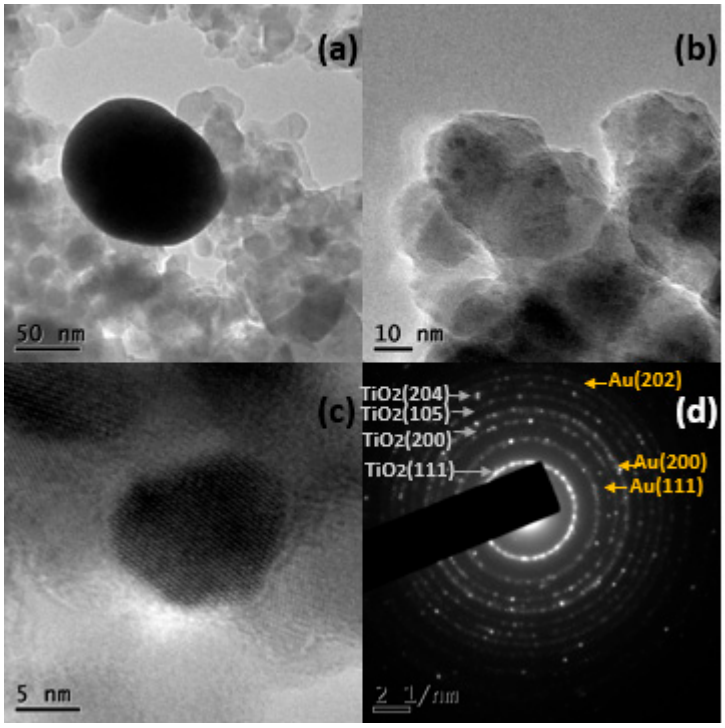

Figure 7. (**a**,**b**) TEM micrographs of 10% Au/TiO_2, (**c**) Au nanoparticle on TiO_2 and (**d**) SAED pattern.

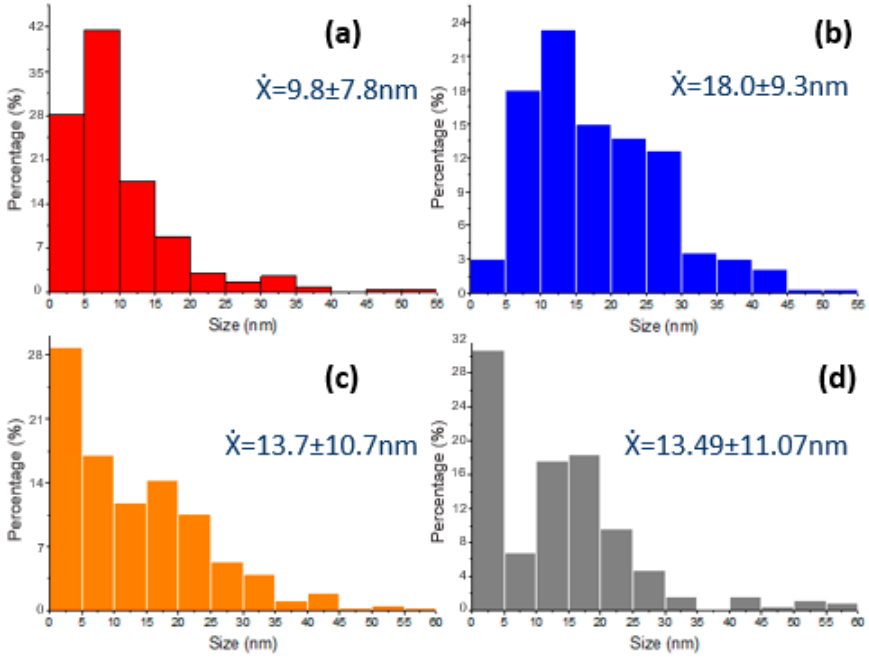

Figure 8. Size distribution histogram of Au nanoparticles for (**a**) 5% Au/BB, (**b**) 10% Au/BB, (**c**) 5% Au/TiO_2 and (**d**) 10% Au/TiO_2 from TEM observations.

The Au-NPs remained supported on the bovine bone and TiO_2 matrices even after being sonicated for a period of 5 h. The results obtained through the TEM technique showed a significant difference in the sizes of Au-NPs on the different supports. While in BB, the Au-NPs did not reach a size larger than 60 nm, in TiO_2, a percentage of the particles showed particle sizes larger than 60 nm, reaching sizes up to 60 nm. Using TiO_2, a percentage of the particles showed larger particle sizes measuring as large as 302 nm. These differences may have been due to the support's texture, with the bovine bone powder having a mesoporous surface [38], which may have limited the growth of the supported nanoparticles and gave them a good polydispersity. At this point, it is important to remember that TiO_2 P25 is a non-porous solid [39].

The characterization results confirmed that the synthesis of Au nanoparticles supported on bovine bone powder and TiO_2 using *Heterotheca inuloides* infusion is a viable solution; the XRD, UV–Vis and TEM techniques demonstrated the presence of Au-NPs supported over BB and TiO_2. The Au-NPs supported on BB showed a decrease in the band gap (2.38 eV for 5% Au and 2.18 eV for 10% Au) compared with pure BB (2.42 eV) (UV–Vis), while for TiO_2, the value did not change significantly. The crystal size obtained using the Scherrer equation, elemental mapping of TEM and TEM micrographs show that the particle sizes of the particles supported on TiO_2 were significantly larger than those supported on BB.

2.1.4. N_2 Physisorption

This analysis was conducted on two of the synthesized materials, 5% Au/BB and 5% Au/TiO_2, and the calculated specific areas by the Brunauer–Emmett–Teller (BET) method were 80.9 and 28.2 m^2/g, respectively. The typical values reported within the literature are ~50 m^2/g for TiO_2 Degussa P25, while the surface area for a bovine bone varies between 36 and 100 m^2/g, depending on different factors like the animal age, treatment (chemical or thermal) and even the part of the animal where the bone was extracted. Nevertheless, from the obtained results, it can be concluded that BB exhibited a higher specific surface area to disperse the metal and for light (photon) absorption.

2.2. Photo-Catalyzed CO_2 Chemical Reduction

Figure 9a–f depicts the effect of the three assessed variables on the methanol, formic acid and acetic acid temporal concentration profiles. It is worth clarifying that in Figure 9a,b, the green line is the only one plotted with respect to the primary Y-axis, while the other ones were plotted with respect to the secondary Y-axis. This was because of the scale difference, i.e., the production with the 5% Au/TiO_2 catalytic system was one order of magnitude higher than with the others. It can be observed that there was a maximum for all cases at relatively short reaction times (within the first 10 min of reaction). Regarding methanol, the highest concentration (24 mmol·g_{cat}^{-1}) was found with the 5% Au/TiO_2 and UV light system (Figure 9b). This value was followed by 20 mmol·g_{cat}^{-1} obtained with the same catalytic system under visible light (Figure 9a), albeit with a shorter reaction time (2 min). The same catalytic system provided the highest concentration (~500 μmol·g^{-1}) of formic acid, also under visible light (Figure 9c). By contrasting Figure 9e,f, it can be observed that when using UV light, the concentration of acetic acid was the highest (~40 μmol·g^{-1}) when using the 5% Au/BB system.

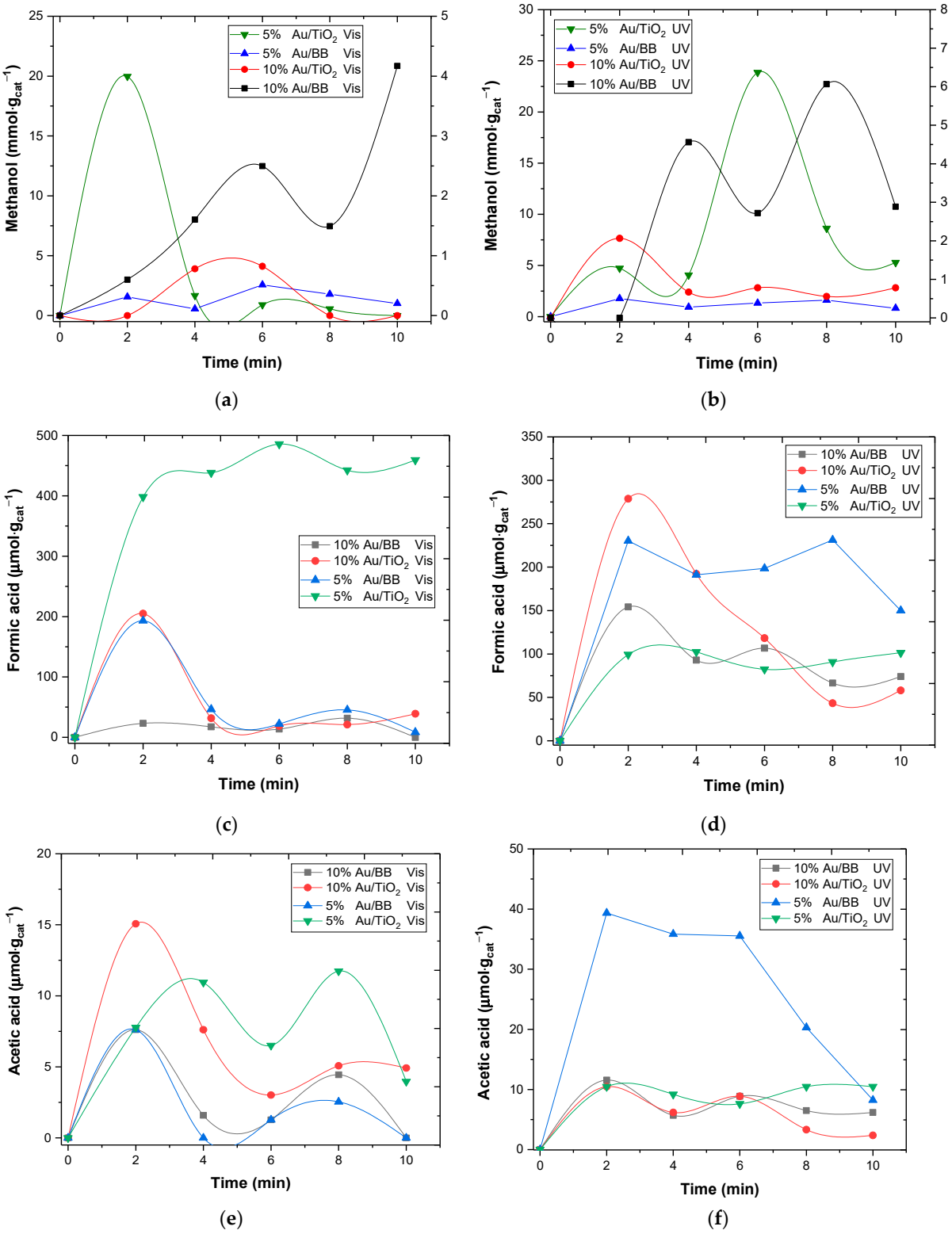

Figure 9. Effect of radiation wavelength, support (BB or TiO_2), and gold content on temporal concentration profiles of methanol, formic acid and acetic acid. (**a**) Temporal concentration profiles of methanol under visible light (green line was plotted on the primary Y-axis); (**b**) temporal concentration profile of methanol under UV light (green line was plotted on the primary Y-axis). (**c**) Temporal concentration profiles of formic acid under visible light and (**d**) UV light. (**e**) Temporal concentration profiles of formic acid under visible light and (**f**) UV light. T = 298 K, W_{cat} = 0.055 g/L, V = 0.1 L, $Q_{CO2} = 9 \times 10^{-3}$ L/min and [NaOH] = 0.5 M.

For TiO_2, it has been acknowledged for a long time that the first step on photocatalyzed CO_2 chemical reduction is the activation of the molecule through electrons transfer on the semiconductor surface, thus forming the carboxylate radical (Equation (1)) [40]:

$$CO_2 \xrightarrow{e^-} *CO_2^- \quad (1)$$

This step was suggested to be followed by protonation and then electron transfer and protonation. Equation (1) does not seem plausible to proceed on bare TiO_2 due to the hydrophilic character of these materials. It was recently claimed, however, that the CO_2 molecule is activated by protons first [41], where such protons likely come from water oxidation onto the photo-generated holes on the semiconductor surface. At this point, it is important to recall the process in this work was conducted under alkaline conditions because the initial reaction solution was 0.5 M NaOH. Under these conditions, upon CO_2 absorption in the alkaline solution, the following reactions proceed and HCO_3^- and CO_3^{2-} ions are produced [42]:

$$CO_2 + OH^- \rightleftharpoons HCO_3^- \quad (2)$$

$$HCO_3^- + OH^- \rightleftharpoons CO_3^{2-} \quad (3)$$

$$CO_2 + H_2O \rightleftharpoons HCO_3^- + H^+ \quad (4)$$

Thus, carbonates and bicarbonates become the reacting species in the studied system. In addition, oxidant species, like hydroxyl radicals, the superoxide radical and hydrogen peroxide, are produced. Hydroxyl radicals are expected to be produced by different means, mainly by the oxidation of water and hydroxyl anions in the generated valence band holes (h^+_{VB}) reactions (5) and (6) in Scheme 2.

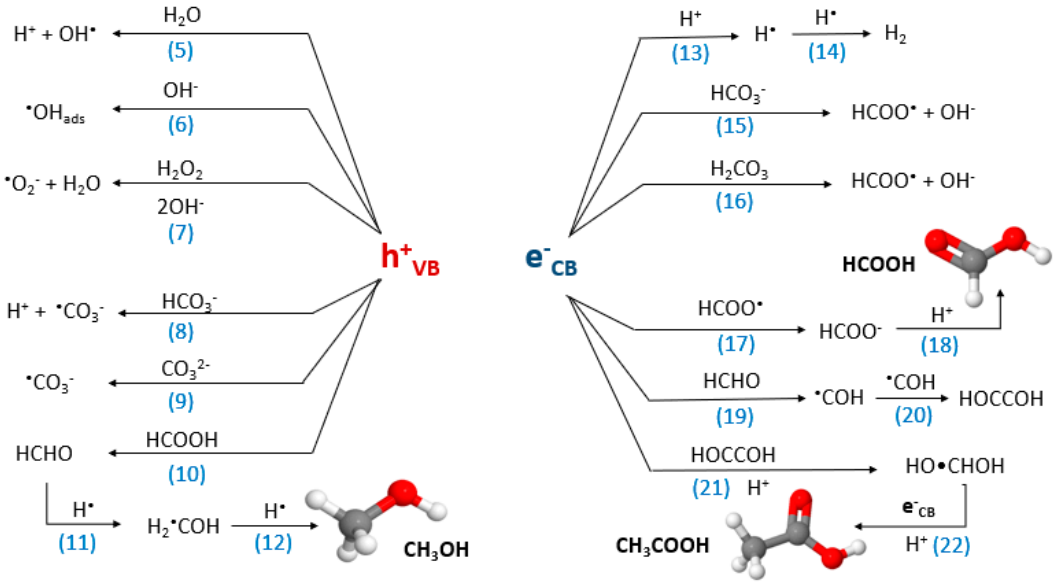

Scheme 2. Plausible reaction pathways to produce methanol, acetic acid and formic acid on TiO_2 surface.

Initially, the hydroxyl anions in reaction 6 might come from the NaOH solution; however, as the process proceeds, these anions are expected to be produced when bicarbonate anions and/or carbonic acid capture a conduction band electron (e^-_{CB}) (Equations (15) and (16)) or react with hydroxyl radicals (reactions (23) and (24)). Hydroxyl radicals react with carbonates and bicarbonates by reactions (23) and (24) [43] to produce the carbonate radical ($^{\bullet}CO_3^-$), which is a strong oxidative radical:

$$HCO_3^- + \cdot OH \rightarrow {}^{\bullet}CO_3^- + H_2O \quad (23)$$

$$CO_3{}^{2-} + \cdot OH \rightarrow {}^{\bullet}CO_3^- + OH^- \quad (24)$$

Although the first produced species is bicarbonate by reaction (2), reaction (3) is relatively instantaneous, and therefore, the main species during the first minutes of the reaction will be carbonates [42], thus favoring reaction (24) instead of (23). In addition, the former has been documented to proceed about 40 times faster than the latter [43].

Reaction Scheme 2 depicts not only the plausible reactions to produce the oxidant and reductor species but also shows a proposed path to produce methanol, formic acid and acetic acid via reactions (11), (12), (15) and (17)–(22) on TiO_2. This is expected [44] for TiO_2; nevertheless, a similar path might be postulated for BB, albeit with some differences.

HAP [$Ca_{10}(PO_4)_6(OH)_2$], which is the main compound in BB, is recognized as a catalyst for acid–base reactions due to the presence of both acidic and basic adsorption sites [45]. Regarding its photoactivity, this can be associated with the defects (OH^-/O^-) in the HAP structure, specifically in the PO_4^{3-} groups, originated by light irradiation. This was demonstrated under UV light [46,47] and based on the results shown in Figure 9; this might also be the case with visible light. In any case, gold is playing an important role because it improves photon absorption in a wide range of the electromagnetic spectrum (see Figure S1a, Supplementary Materials).

The few related manuscripts reporting the CO_2 photoconversion with HAP consider polarized HAP and explain the production of acetic acid and formic acid with the formation of carbon monoxide on the surface, followed by dimerization in the case of acetic acid production [1,4]. In other cases, when polarized HAP was not used, albeit with CO_2 in gas phase, it was demonstrated that carbonates were formed upon CO_2 adsorption on the O^{2-} ions of phosphates and OH^- [10,48]. This step is unlikely to occur in this case because there was no molecular CO_2 in the solution in the first minutes of the reaction; see Figures S3 and S4 (Supplementary Materials) (CO_2 species diagram distribution and temporal pH profiles, respectively). Since the main species was carbonate, and this is a moderately strong base, this could be chemisorbed onto Ca^+ and/or activate via reaction (9) on the photo-generated holes in the valence band (PO_4^{3-}) [10]. At the working pH, the presence of bicarbonates was also expected but to a much lower extent (Figure S3, Supplementary Materials), and thus, reactions (8) and (15) cannot be disregarded.

If hydrogen is being produced via reactions (13) and (14), this can be oxidized at the photo-generated holes in the valence band of either TiO_2 or (PO_4^{3-}) [37]. It must be kept in mind that these holes also participate in the oxidation of water (reaction (5)) and organic molecules. This might be the reason for the decrease in the production rate after, in most of the cases, two minutes of reaction. Nevertheless, methanol is well known as a hydroxyl radical scavenger [49]. Hydroxyl radicals are readily produced by reactions 5 and 6. Thus, the oxidation of methanol, formic acid and acetic acid by hydroxyl radicals is more likely to be responsible for its rapid disappearance within the first minutes of reaction. In addition, it was shown that phosphate ions (Brönsted acid/base sites) enhance the formation of free hydroxyl radicals [50].

It can be observed in Figure 9 that regardless of the Au content, methanol, formic acid and acetic acid were produced. The temporal concentration profiles of each compound, however, were indeed affected by all the assessed variables. In the case of the methanol concentration (Figure 9a,b), the effect of the gold content was positive when BB was used as the support, either under UV or Vis light. This can be ascribed to the BB's ability of absorbing photons in both wavelength ranges (see Figure S1a, Supplementary Materials) and to the gold plasmonic band [51].

Figure 10 depicts the plausible electronic phenomena on the gold and BB surfaces when irradiated by visible light. According to Figure S1 (Supplementary Materials), the BB absorbs the energy of a wide wavelength range in the electromagnetic spectrum. This includes visible light. In the same Figure S1 (Supplementary Materials), for the gold-loaded BB, an absorption peak was observed between 538 and 550 nm. This peak was observed with 5% and 10% gold contents and could be ascribed to the surface plasmon resonance absorption inherent to gold nanoparticles [51]. This characteristic allowed us to

presume that when the Au/BB materials were irradiated by visible light, this was energetic enough to generate electrons that were able to migrate to the support conduction band or to participate in the reactions depicted in Scheme 2. It is worth noticing that under visible light, the photo-generation of the hole–electron pair (h^+–e^-) is expected to also occur on the BB surface.

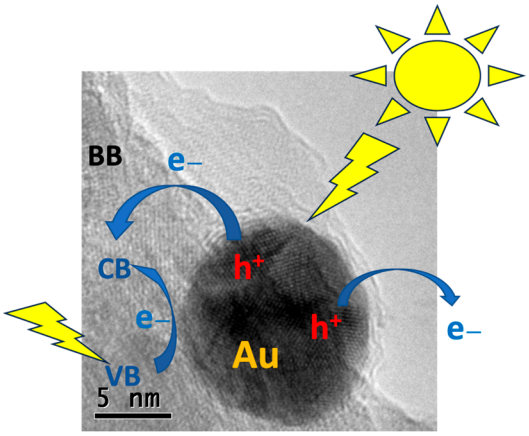

Figure 10. Effect of visible light on gold (black sphere in the image) and bovine bone powder electronic surface phenomena.

Conversely, when titania is part of the catalytic system, visible light will only induce the surface plasmon absorption of gold nanoparticles, and thus, the available electrons for chemical reduction are only those produced in the metal, whilst UV light will photo-generate hole–electron pairs in the TiO_2 and will also activate gold. It can be observed that when using Au/TiO_2, the gold content did not favor the methanol concentration. It only favored the acetic acid concentration under visible light and formic acid under UV light. In both cases and in comparison, with the other catalytic systems, the following maximum concentrations were found: 15 μmol·g^{-1} for the acetic acid and around 280 μmol·g^{-1} in the case of formic acid.

Although still debatable [33] and as referred in the Introduction, in this case, the electrons intervening in the CO_2 chemical reduction might be plasmon hot electrons, which are those from the decay of the surface plasmon [34]. It was claimed that such carriers exhibit a Fermi level above that of the metal, which was gold in this case [34].

Figure 11 shows the effect of the catalytic system composition and applied radiation on selectivity toward methanol after 10 min of reaction, as calculated by the following equation:

$$S = \frac{C_{CH3OH}}{C_{CH3OH} \cdot C_{HCOOH} \cdot C_{CH3COOH}} \times 100$$

where

C_{CH3OH} : *methanol concentration* $(\text{mol}\cdot\text{g}^{-1})$;
C_{HCOOH} : *formic acid concentration* $(\text{mol}\cdot\text{g}^{-1})$;
$C_{CH3COOH}$: *formic acid concentration* $(\text{mol}\cdot\text{g}^{-1})$.

It can be observed in Figure 11 that the selectivity toward methanol was a function of the assessed variables and was the best (100%) when the catalytic system was 10% Au/BB under visible light. This could be attributed to plasmon-driven photocatalysis (PDP) dominating instead of the normal photocatalysis. This could be inferred from the effect of the metal loading and average particle size [52], which was almost double (18.09 ± 9.3 nm) for the 10% Au/BB system than for the 5% Au/BB system (9.8 ± 7.8 nm). In PDP, hot electrons are injected into the semi-conductor surface. Such electrons are produced in the decay of the surface plasmon. Thus, due to the surface plasmon being the main source of electrons for the whole reduction process, i.e., water and organics, the larger the particle and the higher the metal content, the higher the activity [52,53]. It is worth highlighting that

this was the only system able to sustain methanol production in the studied reaction time. In photocatalysis, it was demonstrated, albeit with water reduction [52], that the smaller the metal particle and content, the better the photo-activity because the main role of gold would be helping the charge separation at the semi-conductor surface. In the case of TiO_2, the molecule that was favored by the PDP was acetic acid (see Figure 9e), which might also suggest that water reduction is also favored under such conditions, thus generating more hydrogen and/or protons that allow for obtaining a further reduced organic molecule, such as acetic acid.

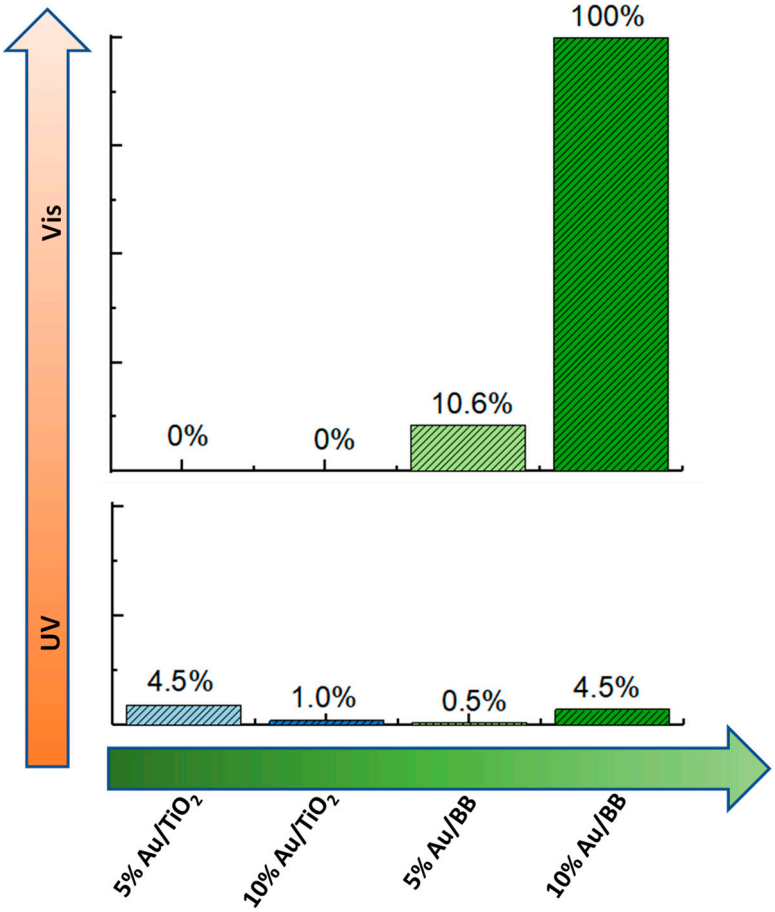

Figure 11. Effects of catalytic system composition and radiation wavelength on selectivity toward methanol. T = 298 K, W_{cat} = 0.055 g/L, V = 0.1 L, $Q_{CO2} = 9 \times 10^{-3}$ L/min, [NaOH] = 0.5 M and t_{rxn} = 10 min.

3. Materials and Methods

3.1. Catalysts Synthesis

In this work, the studied catalytic system was constituted by gold and the support. Two variables were assessed: one was the type of support, and the second one was the gold content in the nanocomposite. Two types of support were used: the typical photocatalyst Degussa P25 (TiO_2), and the other one was a bio-support, bovine bone powder (BB), which is a renewable and biodegradable waste material. The first step in obtaining the bovine bone powder was cleaning the organic residues; then, the BB was placed in contact with 1×10^{-2} M HCl solution, and the BB was pulverized and sieved at 150 mesh. Bionanocomposites, Au/BB and Au/TiO_2, were synthesized with 5% and 10% Au by weight.

Gold nanoparticle synthesis was carried out by bioreduction using an infusion of *Heterotheca inuloides*. For this purpose, 1.5 g of *Heterotheca inuloides* leaves and flowers (purchased in the local market of Metepec, Edo. Mex.) were added in 250 mL of boiling

water for 1 h. H $AuCl_3$ (Meyer, Mexico City, Mexico) solution was prepared at a concentration of 1×10^{-3} M in deionized water. A total of 1 g of bovine bone powder or TiO_2 was immersed in different volumes of $AuCl_3$ solution for 30 s and then filtered. Bovine bone was purchased in a local store located at Plan de Agua Prieta, La Magadalena, 50190, Toluca, Edo. de Mexico, Mexico). Subsequently, Au^{+1} ions were reduced by adding *Heterotheca inuloides* infusions for 1 h under stirring at room temperature and then filtered. The final biocomposites were dried at room temperature. This synthesis was based on previous work carried out by our research group [30,31]. The produced materials are described in Table 1.

Table 1. Synthesized catalysts.

Name	% Au	Support	Immersion Time
BB	0	Bovine bone powder	30 s
5% Au/BB	5	Bovine bone powder	
10% Au/BB	10	Bovine bone powder	
5% Au/TiO_2	5	Titanium dioxide	
10% Au/TiO_2	10	Titanium dioxide	

3.2. Catalyst Characterization

To establish the crystal structure of the composites, X-ray diffraction (XRD) was conducted in a Bruker *D8 Advance* diffractometer with Bragg–Brentano geometry using Cu Kα radiation and a *Linxeye* detector. Optical characterization was carried out by UV–Vis diffuse reflectance spectroscopy in an Ocean Optics DT-1000 CE UV–Vis spectrophotometer. The optical band gap, E_g, was determined using Tauc's expression [54,55]. The Tauc model was plotted based on direct semiconductor using an absorption coefficient $(\alpha)^{1/r}$, where r = 1/2 [56,57]. Scanning electron microscopy (SEM) was used to analyze the morphology and topography; the samples were analyzed in JEOL JSM-6510LV equipment, coupled with an energy dispersive X-ray spectroscopy (EDS) detector from Oxford for the elemental analysis. This equipment was manufactured by JEOL and is located at CCIQS UAEM-UNAM, Toluca, Mexico. The size and shape of Au particles were analyzed by electronic transmission microscopy (TEM) in a JEOL JEM-2100 microscope operated at 200 kV with a LaB_6 filament. This equipment was manufactured by JEOL and is located at CCIQS UAEM-UNAM, Toluca, Mexico. The samples were suspended in 2-propanol and then ultrasonically dispersed for 5 h at room temperature. A drop of this suspension was then placed on a Cu grid coated with a holey carbon film.

N_2 physisorption analyses were conducted for two materials, 5% Au/BB and 5% Au/TiO_2. These materials were elected because, as observed in Section 2, they led to the highest methanol and formic acid concentrations. This analysis was carried out in a Micro 200C equipment. This equipment was manufactured by 3P Instruments and is located at UAM Iztapalapa, Mexico City, Mexico. Samples were degassed for 3 h at 300 °C prior to the analysis.

3.3. Photocatalyzed CO_2 Chemical Reduction

Every catalyst presented in Table 1 was tested in the photo-reduction of CO_2 that was carried out in a Pyrex glass batch photoreactor. The reactor had an inner diameter of 2.5 cm and a height of 20 cm. A 5.5-watt mercury UV Pen-Ray lamp was placed at the reactor center. This lamp required a 115 V/60 Hz power supply and emitted primary radiation at 254 nm with a typical intensity of 4400 μW/cm^2. Every experiment was carried out under constant stirring while a cooling jacket maintained the temperature at 298 K. For the reactions, 100 mL of a 0.5 M NaOH solution and a catalyst loading of 55 mg/L were added to the photoreactor. CO_2 was fed (9.0×10^{-3} dm^3/min) to the reactor through a diffusor placed at the bottom of the reactor, and the experiments were conducted at atmospheric pressure. The lamp was then turned on. Another assessed variable was the radiation

wavelength. For this purpose, a set of three lamps that emitted visible light were placed around the reactor. The response variables were the methanol, formic acid and acetic acid concentrations, and the produced amounts of organic compounds (total organic carbon).

3.4. Analytical Methods

Samples were taken during the photoreduction reaction, passed across a nylon membrane (0.2 μm) to filter out any solid particles (catalysts) and then examined using ultra-high-performance liquid chromatography (UHPLC). A Vanquish system (Thermo Scientific) with refraction index detectors and a diode array (DAD) was utilized for this purpose. With a flow rate of 0.6 mL/min and a mobile phase consisting of 3 mM H_2SO_4, the injection volume was 20 μL. An Aminex HPX-87H BioRad column (9 μm, 7.8 × 300 mm) that operated at a constant temperature of 35 °C was used to achieve separation. This method allowed for the identification and measurement of acetic and formic acids.

In addition, a GC SCION 456 gas chromatograph (GC) with a flame ionization detector (FID) was used to identify and quantify the methanol. The chromatographic column was an Equity TM-1 fused silica capillary with a length of 30 m, diameter of 0.25 mm and a film thickness of 1.0 μm. The analysis conditions were an oven temperature of 35 °C for 2 min, with a temperature ramp of 4 °C/min, 100 °C for 2 min, detector temperature of 250 °C and injector temperature of 250 °C, and a 1 μL injection volume.

4. Conclusions

Gold nanocomposites with 5 and 10% gold contents were synthesized using different supports, BB (bovine bone powder) and TiO_2, by bioreduction using an infusion of *Heterotheca inuloides*. All synthesized materials presented photo-activity in the UV and Vis spectra and could be used as catalysts in the photo-chemical reduction of CO_2 toward methanol, acetic acid and formic acid. The assessed variables (support, gold content and radiation wavelength) were found to exert important effects on the concentrations of the above-said organic compounds. The maximum produced amount of methanol was 24 mmol·g_{cat}^{-1} with the catalytic system of 5% Au/TiO_2 under UV light after six minutes of reaction, followed by the same catalytic system, albeit under visible light. The latter also favored formic acid production, and a maximum of nearly 500 μmol·g_{cat}^{-1} was observed. The acetic acid concentration was favored by using the 5% Au/BB catalytic system under UV light, and a maximum concentration of 40 μmol·g_{cat}^{-1} was quantified. It was concluded that under visible light, plasmon-driven photocatalysis dominated the process.

Finally, it could be concluded that selectivity toward methanol was also affected by all the assessed variables, and at ten minutes of reaction, the highest (100%) was found with 10% Au/BB under visible light. This makes bovine bone powder an interesting material with potential application in the selective reduction of CO_2 in the liquid phase toward methanol under visible light.

Supplementary Materials: The following supporting information can be downloaded from https://www.mdpi.com/article/10.3390/catal14070417/s1: Figure S1: (a) UV–Vis DRS spectra of Au-NPs supported on a BB (5% blue and 10% red) sample, as well as the bare BB (violet). Tauc plot of (b) 5% Au-NPs and (c) 10% Au-NPs supported on BB samples for band gap value determination; Figure S2: (a) Absorption UV–Vis spectra of Au-NPs supported on a TiO_2 (5% red and 10% blue) sample, as well as the bare BB (black). Tauc plot of (b) 5% Au-NPs and (c) 10% Au-NPs supported on TiO_2 samples for band gap value determination; Figure S3: CO_2 species distribution diagram as function of pH at 295 K. Figure S4: pH temporary profiles: effect of radiation wavelength, gold content and type of support.

Author Contributions: Conceptualization, R.N. and S.A.G.-L.; methodology, R.N., S.A.G.-L., A.R.V.-N. and D.A.-P.; validation, D.A.-P.; formal analysis, R.N., S.A.G.-L., A.R.V.-N. and D.A.-P.; investigation, R.N. and S.A.G.-L.; resources, R.N. and S.A.G.-L.; writing—original draft preparation, S.A.G.-L., A.R.V.-N. and D.A.-P.; writing—review and editing, R.N.; supervision, R.N.; project administration, R.N.; funding acquisition, R.N. All authors have read and agreed to the published version of the manuscript.

Funding: Autonomous University of the State of Mexico (project 7029/2024CIB).

Data Availability Statement: The data presented in this study are available upon request from the corresponding author. The raw data required to reproduce these findings cannot be shared at this time as the data also form part of an ongoing study.

Acknowledgments: The technical support of Citlalit Martinez Soto and Sharon Lizeth Tenorio is acknowledged. D. Amado-Piña is grateful to CONAHCYT for financial support.

Conflicts of Interest: The authors declare no conflicts of interests.

References

1. Arnau, M.; Turon, P.; Alemán, C.; Sans, J. Hydroxyapatite-based catalysts for CO_2 fixation with controlled selectivity towards C2 products. Phenomenal support or active catalyst? *J. Mater. Chem. A* **2022**, *11*, 1324–1334. [CrossRef]
2. Sans, J.; Arnau, M.; Turon, P.; Alemán, C. Permanently polarized hydroxyapatite, an outstanding catalytic material for carbon and nitrogen fixation. *Mater. Horizons* **2022**, *9*, 1566–1576. [CrossRef]
3. Sans, J.; Revilla-López, G.; Sanz, V.; Puiggalí, J.; Turon, P.; Alemán, C. Permanently polarized hydroxyapatite for selective electrothermal catalytic conversion of carbon dioxide into ethanol. *Chem. Commun.* **2021**, *57*, 5163–5166. [CrossRef] [PubMed]
4. Lv, C.; Liang, H.; Chen, H.; Wu, L. Hydroxyapatite supported Co_3O_4 catalyst for enhanced degradation of organic contaminants in aqueous solution: Synergistic visible-light photo-catalysis and sulfate radical oxidation process. *Microchem. J.* **2019**, *149*, 103959. [CrossRef]
5. Shu, K.; Chuaicham, C.; Noguchi, Y.; Xu, L.; Sasaki, K. In-situ hydrothermal synthesis of Fe-doped hydroxyapatite photocatalyst derived from converter slag toward xanthate photodegradation and Cr(VI) reduction under visible-light irradiation. *Chem. Eng. J.* **2023**, *459*, 141474. [CrossRef]
6. Liu, X.; Ma, J.; Yang, J. Visible-light-driven amorphous Fe(III)-substituted hydroxyapatite photocatalyst: Characterization and photocatalytic activity. *Mater. Lett.* **2014**, *137*, 256–259. [CrossRef]
7. Kalita, J.; Das, B.; Dhar, S.S. Synergistic effect of iron and copper in hydroxyapatite nanorods for Fenton-like oxidation of organic dye. *Colloids Surfaces A Physicochem. Eng. Asp.* **2022**, *643*, 128750. [CrossRef]
8. de Medeiros, F.G.M.; Farzi, F.; Achouri, I.E.; Lotfi, S.; de Vasconcelos, B.R. Performance of Hydroxyapatite-Supported Catalysts for Methane Production Via CO_2 Hydrogenation on Semi-Pilot Scale. *Waste Biomass-Valorization* **2023**, *14*, 3429–3444. [CrossRef]
9. Sans, J.; Sanz, V.; Turon, P.; Alemán, C. Enhanced CO_2 Conversion into Ethanol by Permanently Polarized Hydroxyapatite through C–C Coupling. *ChemCatChem* **2021**, *13*, 5025–5033. [CrossRef]
10. Dos Santos Silva, D.; Villegas, A.E.C.; Bonfim, R.D.P.F.; Salim, V.M.M.; De Resende, N.S. Iron-substituted hydroxyapatite as a potential photocatalyst for selective reduction of CO_2 with H2. *J. CO2 Util.* **2022**, *63*, 102102. [CrossRef]
11. Tran, N.D.T.; Che, T.N.H.; Van Nguyen, T.T.; Do, B.L.; Ho, T.G.T.; Nguyen, P.A.; Pham, T.T.P.; Tri, N.; Ha, H.K.P. Fishbone derived-hydroxyapatite supported Ni-Zr nanocatalyst for CO_2 methanation: Synergistic effects of support and zirconia. *Arab. J. Chem.* **2023**, *16*, 105307. [CrossRef]
12. Phan, T.S.; Sane, A.R.; de Vasconcelos, B.R.; Nzihou, A.; Sharrock, P.; Grouset, D.; Minh, D.P. Hydroxyapatite supported bimetallic cobalt and nickel catalysts for syngas production from dry reforming of methane. *Appl. Catal. B* **2018**, *224*, 310–321. Available online: https://hal.science/hal-01630309 (accessed on 24 February 2024). [CrossRef]
13. Rego de Vasconcelos, B.; Pham Minh, D.; Martins, E.; Germeau, A.; Sharrock, P.; Nzihou, A. Highly-efficient hydroxyapatite-supported nickel catalysts for dry reforming of methane. *Int. J. Hydrog. Energy* **2020**, *45*, 18502–18518. [CrossRef]
14. Wang, Q.-N.; Weng, X.-F.; Zhou, B.-C.; Lv, S.-P.; Miao, S.; Zhang, D.; Han, Y.; Scott, S.L.; Schüth, F.; Lu, A.-H. Direct, Selective Production of Aromatic Alcohols from Ethanol Using a Tailored Bifunctional Cobalt–Hydroxyapatite Catalyst. *ACS Catal.* **2019**, *9*, 7204–7216. [CrossRef]
15. Hua, M.; Song, J.; Xie, C.; Wu, H.; Hu, Y.; Huang, X.; Han, B. Ru/hydroxyapatite as a dual-functional catalyst for efficient transfer hydrogenolytic cleavage of aromatic ether bonds without additional bases. *Green Chem.* **2019**, *21*, 5073–5079. [CrossRef]
16. Li, S.; Li, Y.; Shen, W.; Bai, Y.; Kong, L. Hydroxyapatite-based catalysis in environmental decontamination. *J. Clean. Prod.* **2022**, *380*, 134961. [CrossRef]
17. Wakamura, M.; Tanaka, H.; Naganuma, Y.; Yoshida, N.; Watanabe, T. Surface structure and visible light photocatalytic activity of titanium–calcium hydroxyapatite modified with Cr(III). *Adv. Powder Technol.* **2011**, *22*, 498–503. [CrossRef]
18. Zou, R.; Xu, T.; Lei, X.; Wu, Q.; Xue, S. Novel and efficient red phosphorus/hollow hydroxyapatite microsphere photocatalyst for fast removal of antibiotic pollutants. *J. Phys. Chem. Solids* **2020**, *139*, 109353. [CrossRef]
19. Kandori, K.; Yamaguchi, Y.; Wakamura, M. Photodecomposition of surfactants using Ti(IV)-doped calcium hydroxyapatite particles. *Colloid Polym. Sci.* **2017**, *295*, 1079–1087. [CrossRef]
20. Nishikawa, H. A high active type of hydroxyapatite for photocatalytic decomposition of dimethyl sulfide under UV irradiation. *J. Mol. Catal. A Chem.* **2004**, *207*, 149–153. [CrossRef]
21. Nishikawa, H.; Kato, S.; Ando, T. Rapid and complete oxidation of acetaldehyde on TiO_2 photocatalytic filter supported by photo-induced activated hydroxyapatite. *J. Mol. Catal. A Chem.* **2005**, *236*, 145–148. [CrossRef]

22. Bharadwaz, A.; Jayasuriya, A.C. Recent trends in the application of widely used natural and synthetic polymer nanocomposites in bone tissue regeneration. *Mater. Sci. Eng. C* **2020**, *110*, 110698. [CrossRef] [PubMed]
23. Camargo, P.H.C.; Satyanarayana, K.G.; Wypych, F. Nanocomposites: Synthesis, structure, properties and new application opportunities. *Mater. Res.* **2009**, *12*, 1–39. [CrossRef]
24. Lateef, A.; Nazir, R. Metal Nanocomposites: Synthesis, Characterization and their Applications. *Sci. Appl. Tailored Nanostructures* **2017**, 239–256.
25. Ali, A.; Shah, T.; Ullah, R.; Zhou, P.; Guo, M.; Ovais, M.; Tan, Z.; Rui, Y. Review on Recent Progress in Magnetic Nanoparticles: Synthesis, Characterization, and Diverse Applications. *Front. Chem.* **2021**, *9*, 629054. [CrossRef] [PubMed]
26. Mikhailova, E.O. Gold Nanoparticles: Biosynthesis and Potential of Biomedical Application. *J. Funct. Biomater.* **2021**, *12*, 70. [CrossRef] [PubMed]
27. Chopra, H.; Bibi, S.; Singh, I.; Hasan, M.M.; Khan, M.S.; Yousafi, Q.; Baig, A.A.; Rahman, M.; Islam, F.; Bin Emran, T.; et al. Green Metallic Nanoparticles: Biosynthesis to Applications. *Front. Bioeng. Biotechnol.* **2022**, *10*, 874742. [CrossRef] [PubMed]
28. Saravanan, A.; Kumar, P.S.; Karishma, S.; Vo, D.V.N.; Jeevanantham, S.; Yaashikaa, P.R.; George, C.S. A review on biosynthesis of metal nanoparticles and its environmental applications. *Chemosphere* **2021**, *264*, 128580. [CrossRef] [PubMed]
29. Hing, K.A.; Best, S.M.; Bonfield, W. Characterization of porous hydroxyapatite. *J. Mater. Sci. Mater. Med.* **1999**, *10*, 135–145. [CrossRef]
30. Gama-Lara, S.A.; Mendoza, M.S.P.; Vilchis-Nestor, A.R.; Natividad, R. Bionanotechnology: Silver Nanoparticles Supported on Bovine Bone Powder Used as Bactericide. *Materials* **2020**, *13*, 462. [CrossRef]
31. Gama-Lara, S.A.; Natividad, R.; Vilchis-Nestor, A.R.; López-Castañares, R.; García-Orozco, I.; Gonzalez-Pedroza, M.G.; Morales-Luckie, R.A. Ultra-Small Platinum Nanoparticles with High Catalytic Selectivity Synthesized by an Eco-friendly Method Supported on Natural Hydroxyapatite. *Catal. Lett.* **2019**, *149*, 3447–3453. [CrossRef]
32. Natividad, R. CO_2 photoconversion catalyzed by nanoparticles supported on TiO_2. In *Nanoparticles in Green Organic Synthesis: Strategy towards Sustainability*; Elsevier: Amsterdam, The Netherlands, 2023; pp. 421–452.
33. Dey, A.; Silveira, V.R.; Vadell, R.B.; Lindblad, A.; Lindblad, R.; Shtender, V.; Görlin, M.; Sá, J. Exploiting hot electrons from a plasmon nanohybrid system for the photoelectroreduction of CO_2. *Commun. Chem.* **2024**, *7*, 59. [CrossRef]
34. Rossi, T.P.; Erhart, P.; Kuisma, M. Hot-carrier generation in plasmonic nanoparticles: The importance of atomic structure. *ACS Nano* **2020**, *14*, 9963–9971. [CrossRef] [PubMed]
35. Mariappan, A.; Pandi, P.; Rani, K.B.; Rajeswarapalanichamy; Neyvasagam, K. Study of the photocatalytic and antibacterial effect of Zn and Cu doped hydroxyapatite. *Inorg. Chem. Commun.* **2021**, *136*, 109128. [CrossRef]
36. Sarina, S.; Waclawik, E.R.; Zhu, H. Photocatalysis on supported gold and silver nanoparticles under ultraviolet and visible light irradiation. *Green Chem.* **2013**, *15*, 1814–1833. [CrossRef]
37. Tsvetkov, M.; Zaharieva, J.; Milanova, M. Ferrites, modified with silver nanoparticles, for photocatalytic degradation of malachite green in aqueous solutions. *Catal. Today* **2019**, *357*, 453–459. [CrossRef]
38. Patel, S.; Han, J.; Qiu, W.; Gao, W. Synthesis and characterisation of mesoporous bone char obtained by pyrolysis of animal bones, for environmental application. *J. Environ. Chem. Eng.* **2015**, *3*, 2368–2377. [CrossRef]
39. De Witte, K.; Ribbens, S.; Meynen, V.; De Witte, I.; Ruys, L.; Cool, P.; Vansant, E.F. Photocatalytic study of P25 and mesoporous titania in aqueous and gaseous environment. *Catal. Commun.* **2008**, *9*, 1787–1792. [CrossRef]
40. Neatu, S.; Maciá-Agulló, J.A.; Concepción, P.; Garcia, H. Gold-copper nanoalloys supported on TiO_2 as photocatalysts for CO_2 reduction by water. *J. Am. Chem. Soc.* **2014**, *136*, 15969–15976. [CrossRef]
41. Yin, S.; Zhou, Y.; Liu, Z.; Wang, H.; Zhao, X.; Zhu, Z.; Yan, Y.; Huo, P. Elucidating protonation pathways in CO_2 photoreduction using the kinetic isotope effect. *Nat. Commun.* **2024**, *15*, 437. [CrossRef]
42. Morales, D.O.; Regalado-Méndez, A.; Pérez-Alonso, C.; Natividad, R. Physical and reactive absorption of CO_2 in capillaries: Mass transfer, modelling and produced chemical species. *Chem. Eng. Res. Des.* **2023**, *198*, 247–258. [CrossRef]
43. Buxton, G.V.; Elliott, A.J. Rate Constant for Reaction of Hydroxyl Radicals with Bicarbonate Ions? *Int. J. Radiat. Appl. Instrum. Part C. Radiat. Phys. Chem.* **1986**, *27*, 241–243. [CrossRef]
44. Karamian, E.; Sharifnia, S. On the general mechanism of photocatalytic reduction of CO_2. *J. CO2 Util.* **2016**, *16*, 194–203. [CrossRef]
45. Bittencourt, A.F.B.; Mendes, P.C.D.; Valença, G.P.; Da Silva, J.L.F. Acid-base properties of hydroxyapatite(0001) by the adsorption of probe molecules: An ab initio investigation. *Phys. Rev. Mater.* **2021**, *5*, 075003. [CrossRef]
46. Nishikawa, H. Photo-Induced Catalytic Activity of Hydroxyapatite Based on Photo-Excitation. *Phosphorus Res. Bull.* **2007**, *21*, 97–102. [CrossRef]
47. Bystrov, V.; Piccirillo, C.; Tobaldi, D.; Castro, P.; Coutinho, J.; Kopyl, S.; Pullar, R. Oxygen vacancies, the optical band gap (Eg) and photocatalysis of hydroxyapatite: Comparing modelling with measured data. *Appl. Catal. B Environ.* **2016**, *196*, 100–107. [CrossRef]
48. Diallo-Garcia, S.; Osman, M.B.; Krafft, J.-M.; Casale, S.; Thomas, C.; Kubo, J.; Costentin, G. Identification of Surface Basic Sites and Acid–Base Pairs of Hydroxyapatite. *J. Phys. Chem. C* **2014**, *118*, 12744–12757. [CrossRef]
49. Wang, L.; Li, B.; Dionysiou, D.D.; Chen, B.; Yang, J.; Li, J. Overlooked Formation of H_2O_2 during the Hydroxyl Radical-Scavenging Process When Using Alcohols as Scavengers. *Environ. Sci. Technol.* **2022**, *56*, 3386–3396. [CrossRef]
50. Ding, L.; Li, M.; Zhao, Y.; Zhang, H.; Shang, J.; Zhong, J.; Sheng, H.; Chen, C.; Zhao, J. The vital role of surface Brönsted acid/base sites for the photocatalytic formation of free ·OH radicals. *Appl. Catal. B Environ.* **2020**, *266*, 118634. [CrossRef]

51. Mondal, S.; Reyes, M.E.; Pal, U. Plasmon induced enhanced photocatalytic activity of gold loaded hydroxyapatite nanoparticles for methylene blue degradation under visible light. *RSC Adv.* **2017**, *7*, 8633–8645. [CrossRef]
52. Qian, K.; Sweeny, B.C.; Johnston-Peck, A.C.; Niu, W.; Graham, J.O.; DuChene, J.S.; Qiu, J.; Wang, Y.-C.; Engelhard, M.H.; Su, D.; et al. Surface Plasmon-Driven Water Reduction: Gold Nanoparticle Size Matters. *J. Am. Chem. Soc.* **2014**, *136*, 9842–9845. [CrossRef] [PubMed]
53. Jiang, D.; Wang, W.; Sun, S.; Zhang, L.; Zheng, Y. Equilibrating the Plasmonic and Catalytic Roles of Metallic Nanostructures in Photocatalytic Oxidation over Au-Modified CeO_2. *ACS Catal.* **2014**, *5*, 613–621. [CrossRef]
54. Makuła, P.; Pacia, M.; Macyk, W. How To Correctly Determine the Band Gap Energy of Modified Semiconductor Photocatalysts Based on UV–Vis Spectra. *J. Phys. Chem. Lett.* **2018**, *9*, 6814–6817. [CrossRef] [PubMed]
55. Kumar, R.; Ali, S.A.; Mahur, A.; Virk, H.; Singh, F.; Khan, S.; Avasthi, D.; Prasad, R. Study of optical band gap and carbonaceous clusters in swift heavy ion irradiated polymers with UV–Vis spectroscopy. *Nucl. Instrum. Methods Phys. Res. Sect. B* **2008**, *266*, 1788–1792. [CrossRef]
56. Escobedo-Morales, A.; Ruiz-López, I.I.; Ruiz-Peralta, M.D.; Tepech-Carrillo, L.; Sánchez-Cantú, M.; Moreno-Orea, J.E. Automated method for the determination of the band gap energy of pure and mixed powder samples using diffuse reflectance spectroscopy. *Heliyon* **2019**, *5*, e01505. [CrossRef]
57. Morales, A.E.; Mora, E.S.; Pal, U. Use of diffuse reflectance spectroscopy for optical characterization of un-supported nanostructures. *Rev. Mex. Fis.* **2006**, *53*, 18–22.